# Structural impact on the nanoscale optical properties of InGaN core-shell nanorods

*J.T. Griffiths*[1], C.X. Ren[1], P.-M. Coulon[2], E.D. Le Boulbar[2], C.G. Bryce[3], I. Girgel[2], A. Howkins[4], I. Boyd[4], R.W. Martin[3], D.W.E. Allsopp[2], P.A. Shields[2], C.J. Humphreys[1], and R.A. Oliver[1]*

1. Department of Materials Science and Metallurgy, Charles Babbage Road, Cambridge, CB3 0FS, United Kingdom

2. Department of Electronic and Electrical Engineering, University of Bath, Bath, BA2 7AY, United Kingdom

3. Department of Physics, SUPA, University of Strathclyde, Glasgow, G4 0NG, United Kingdom

4. Experimental Techniques Centre, Brunel University, Uxbridge, UB8 7BQ, United Kingdom

III-nitride core-shell nanorods are promising for the development of high efficiency light emitting diodes and novel optical devices. We reveal the nanoscale optical and structural properties of core-shell InGaN nanorods formed by combined top-down etching and regrowth to achieve non-polar sidewalls with a low density of extended defects. Whilst the luminescence is uniform along the non-polar {1-100} sidewalls, nano-cathodoluminescence shows a sharp reduction in the luminescent intensity at the intersection of the non-polar {1-100} facets. The reduction in the luminescent intensity is accompanied by a reduction in the emission energy localised at the apex of the corners. Correlative compositional analysis reveals an increasing indium content towards the corner except at the apex itself. We propose that the observed variations in the structure and chemistry are responsible for the changes in the optical properties at the corners of the nanorods. The insights revealed by nano-cathodoluminescence will aid in the future development of higher efficiency core-shell nanorods.

KEYWORDS (4-6 words) Core-shell nanorods, optoelectronics, light emitting diodes, III-nitrides, nano-cathodoluminescence

III-nitride semiconductors exhibit high luminous efficiencies and have led to the development of high efficiency short wavelength optical devices [1]. They show particularly high efficiencies over the blue spectral region, which has led to the development of white light emitting diodes with superior energy efficiencies relative to traditional forms of lighting [2,3]. Quantum wells are often used to confine the carriers to increase the radiative recombination rate, however improvements in traditional polar quantum wells are hampered by the strong polarisation fields along the polar axis [4]. The polarisation fields lead to the spatial separation of the electrons and holes leading to a reduction in device efficiency, known as the quantum confined Stark effect (QCSE) [5]. This effect also contributes to higher carrier densities at the higher powers required for general lighting leading to increasingly large reductions in device efficiency from 'efficiency droop' [6]. The negative impact of the polarisation field can be suppressed though by growth in orientations perpendicular to the polar direction, known as non-polar orientations [7,8]. However, planar growth along non-polar orientations leads to a large number of non-radiative defects [9] unless grown on expensive native substrates.

Core-shell InGaN nanorods offer low defect density, non-polar sidewalls [10–12] on cheap foreign substrates. Thicker active regions may be grown [13] without leading to large spatial separations between the electrons and holes due to the mitigation of the QCSE. The combination of larger effective light emitting area and improved radiative efficiency provides scope for substantial reductions in the local carrier density, leading to a potential reduction in efficiency droop and ultimately higher efficiency light emitting devices. The unique 3D nanostructure also offers the potential for the development of quantum dots [14–16], which can provide novel optical properties.

However, the development of high efficiency nanostructures requires understanding and control of the structural and optical properties at the nanoscale. Cathodoluminescence (CL)

spectroscopy offers the capability to study the optical properties with high spatial resolution. Recently, by performing CL in a scanning transmission electron microscope (STEM) it has been possible to study nanoscale optical properties down to just a few nanometres [17,18] and reveal simultaneously the structural and chemical properties, an approach that is commonly referred to as nano-cathodoluminescence (nano-CL). This method has already shown great success in the characterisation of pure GaN nanocolumns [19], InGaN nanodisk-rod structures [20], and recently variations in the emission energy along the sidewalls of InGaN core-shell nanorods [21].

In this letter, nano-CL is applied to reveal the highly spatially resolved optical properties of InGaN core-shell nanorods and variations in the luminescence intensity and emission energy. We correlate the variations in the optical characteristics with the structural and chemical properties on the nanoscale to reveal insights into the origin of spatial variations in their luminescence.

Nanorod arrays were fabricated using a combined top-down etching and regrowth approach, with the final nanorod array schematically shown in figure 1a. Nanolithography and a lift-off process were used to create a hexagonal array of nickel dots with a diameter of 500 nm and a pitch of 2 μm on a (0001) GaN on silicon template [22]. Subsequently, a GaN/AlN/Si nanorod array was fabricated by inductively coupled plasma (ICP) etching using a $Cl_2$/Ar gas mixture. Prior to the metal organic vapour phase epitaxy (MOVPE) regrowth, the etched nanorod array was subjected to an in-situ nitridation step at 950 $^{o}$C to create a $SiN_x$ passivation layer at the silicon surface and prevent gallium melt-back etching. MOVPE GaN faceting regrowth was performed at 900 $^{o}$C to recover smooth and regular {1-100} non-polar and {1-101} semi-polar facets [23]. Finally, the faceted GaN nanorods were overgrown with a single 11 nm wide InGaN shell at 685 $^{o}$C, followed by the growth of a GaN cap layer.

The scanning electron microscope (SEM) image presented in figure 1b shows a uniform hexagonal array of nanorods with a density of $2.9 \times 10^5$ nanorods/mm$^2$. From the SEM image, each of the nanorods comprises six smooth {1-100} non-polar side walls along with six semi-polar {1-101} facets at the tips, indicated in the inset of figure 1b. Some nanorods retain a polar (0001) surface that intersects the {1-101} semi-polar facets at the tip. The height and diameter of the nanorods is 1.8 and 0.8 μm respectively, corresponding to an aspect ratio of 2.25.

The CL spectrum (figure 1c) integrated over an individual nanorod reveals the InGaN emission peak centred at 2.56 eV, with a broad 236 meV linewidth. Representative spectra from the polar, semi-polar, and non-polar facets from the regions marked by the circles in the inset SEM image are also shown in figure 1c. The emission spectra from each of the facets are relative to the non-polar facet and reveals that the peak emission is more than an order of magnitude more intense than from the other facets and dominates the nanorod emission. The brighter intensity from the non-polar sidewalls may arise from the mitigation of the internal electric fields leading to stronger overlap of the electron and hole wavefunctions as well as from the optimised growth parameters [25]. The lowest energy emission, at a peak energy ~2.48 eV, arises from the polar tips of the nanorods, whilst there is an increase in the peak energy of the emission from the semi-polar facets to 2.53 eV. The non-polar side walls exhibit the highest emission peak energy at 2.58 eV. The low energy tail below 2.2 eV is attributed to the defect states caused by the unintentional incorporation of impurities [24].

To reveal the variation in the optical characteristics along the nanorod, CL hyperspectral imaging in a SEM was performed at an accelerating voltage of 5 kV with 5.5 nA to capture room temperature CL with a 40 nm pixel size, where each pixel corresponds to a localised CL spectrum. Variations in the local emission intensity and emission energy are shown in figure 1d

and 1e respectively. Whilst the brightest luminescence arises from the non-polar sidewalls, there is a reduction in luminescence intensity along the entire length at the intersection of the sidewalls. The peak emission energy also red-shifts by 55 meV at the intersections of the non-polar sidewalls relative to the sidewalls along the entire length of the nanorods. The emission energy along the length of the non-polar sidewalls though varies by less than 30 meV for the growth parameters used here [26].

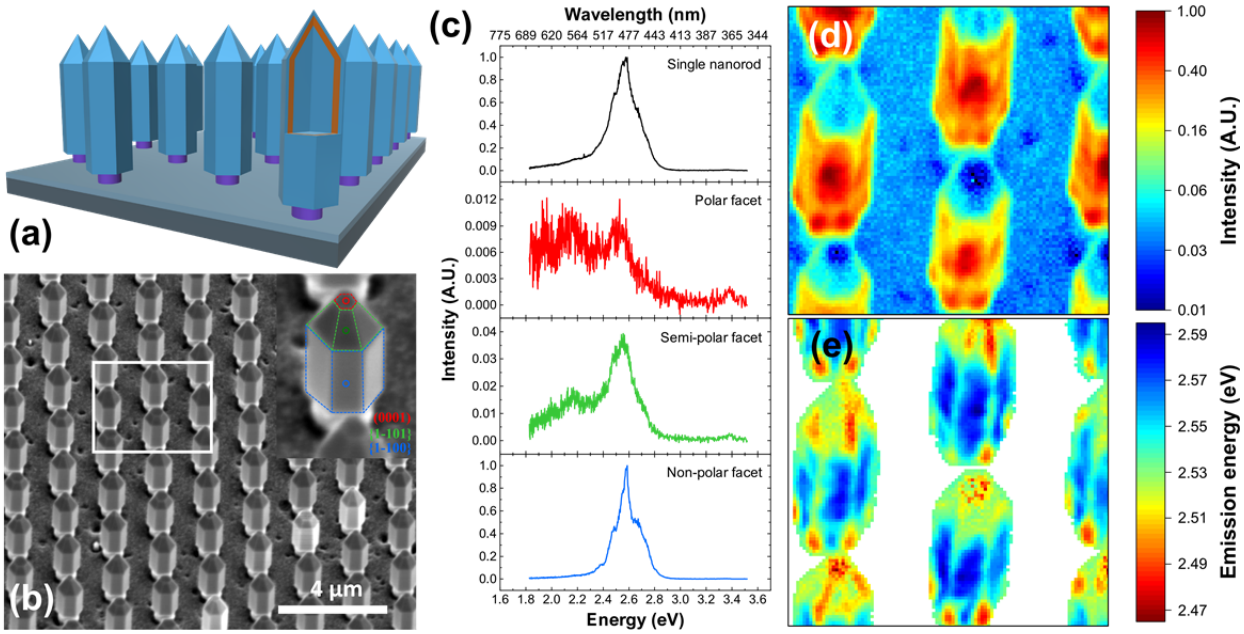


Figure 1. (a) Schematic of a nanorod array. A slice through the foremost nanorod reveals the GaN core in blue, the surrounding InGaN shell in orange and the GaN capping layer also in blue. The etched AlN core layer is represented in purple on top of the $SiN_x$ passivation layer (light grey) on the silicon substrate (dark grey). (b) SEM image of the nanorod array, with an inset image of a nanorod indicating the {1-100} non-polar sidewalls in blue, the {1-101} semi-polar facets in green and the (0001) polar surface in red. (c) Room temperature CL emission average spectrum from a single nanorod with a peak emission energy at 2.56 eV. The spectra from the polar, semi-polar and non-polar facets identified by the circles in the inset of the SEM image,

and are all relative to the non-polar spectrum. Room temperature hyperspectral CL images of (d) the intensity and (e) peak emission energy from 2.59 eV to 2.46 eV from the region indicated by the white box on the SEM image.

To study the variation in the optical and structural properties at the intersection of the non-polar sidewalls through the InGaN shell and in further detail, an axial cross-section at the centre of a nanorod was prepared by focussed ion beam (FIB) to view along the polar axis for STEM. Hydrogen silsesquioxane (HSQ) was first spun onto the nanorods to embed and protect them from damage. FIB was used to prepare hexagonal nanorods sections using 30 keV gallium ions with a final 5 keV polishing step, leading to a lamella containing several nanorods.

The nanoscale optical characteristics were studied by nano-CL using a JEOL 2100F Schottky field emission gun TEM fitted with a Gatan Vulcan CL system using a 0.5 nm electron probe with 13 pA. An 80 keV accelerating voltage was used to reduce the effects of electron beam induced damage [27]. The sample was cooled down to 100 K leading to a blue-shift in emission energy relative to the room temperature SEM-CL analysis. The panchromatic nano-CL image shown in figure 2a reveals the brighter emission associated with the non-polar InGaN sidewalls and the quenching of the emission at the corners of nanorods. The variation in the panchromatic intensity reflects the variations previously observed by SEM-CL, but shows more clearly the localised nature of the intensity variation.

CL emission spectrum from the centre of a non-polar sidewall shown in figure 2b (blue circle in figure 2a) shows a central emission peak at 2.72 eV with a 243 meV linewidth. In contrast, the emission spectrum at the corner of the nanorod (green circle in figure 2a) is red-shifted by 60 meV, with a narrower 170 meV linewidth.

To investigate the variations in the optical properties at the nanoscale, hyperspectral imaging was performed at the corner of a nanorod represented by the orange square in figure 2a, to reveal localised variations in intensity and emission energy with a 5 nm pixel size and each pixel acquired for 0.5 s. The peak intensity map (figure 2c) shows the extent of the luminescence quenching at one of the corners of the nanorod. The peak emission energy map (figure 2d) further shows that the inner part of the corner exhibits a red-shift of approximately 60 meV, which further decreases in emission energy towards the apex to 140 meV relative to the sidewalls.

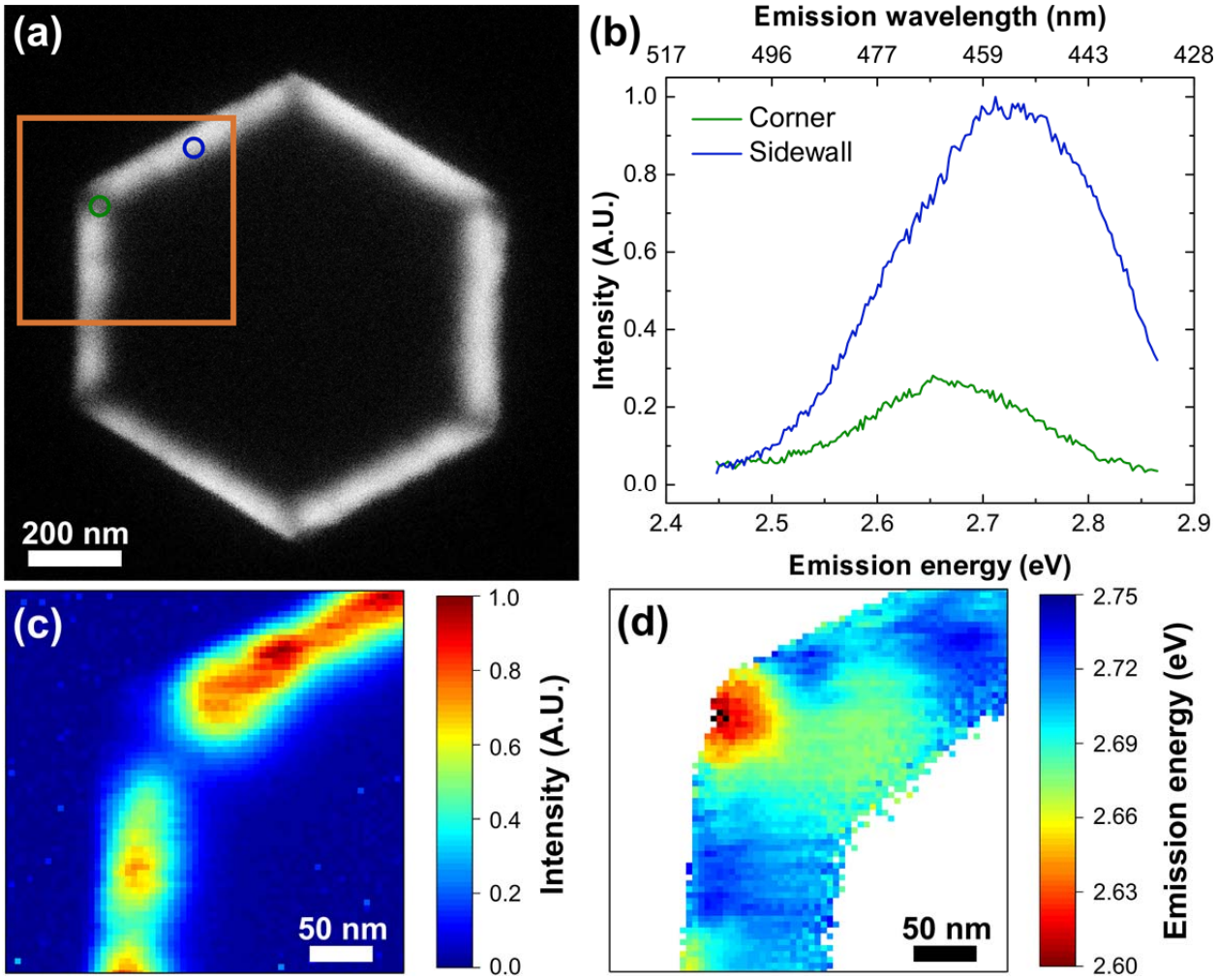

Figure 2. (a) Panchromatic nano-CL image of a nanorod in cross-section viewed along the polar axis. (b) The CL emission spectra from the centre of a non-polar side wall and from the centre of a corner. Hyperspectral imaging was performed around the corner of the nanorod to reveal (c) the emission intensity and (d) the emission energy.

The origin of the reduction in the luminescent intensity was studied by atomic resolution STEM. Figure 3a shows the annular dark field (ADF) STEM image of a nanorod where InGaN shows bright contrast relative to GaN. The overview of the nanorod shows dislocations propagating towards the sidewalls as the regrowth induces bending of dislocations originating from within the GaN etch core. No additional extended defects are observed at the interface between the InGaN shell and the GaN, either at the non-polar sidewalls or at the intersections.

The higher resolution STEM image of the corner of the nanorod reveals the existence of a residual non-polar {11-20} facet on the GaN core, indicating that the initial GaN overgrowth of the etched nanorods was not sufficient to form six-sided structures bounded by the slow-growing {1-100} facets. The STEM image also shows this residual {11-20} facet reduces as the nanostructure shape evolves owing to a slower growth rate on the bounding {1-100} planes [28].

The variation in the indium content was measured by energy dispersive X-ray spectroscopy (EDS) shown in figure 3c and reveals the variation in the indium distribution around the corner of the nanorod to within one percent of the group-III alloy fraction. On the inner part of the InGaN layer closest to the GaN core, the indium content rises from ~15% on the {1-100} planes to ~22% in the middle of the residual {11-20} plane. However, after about 10 nm of InGaN growth a clear divergence in the InGaN composition occurs in the corner region, with regions of

high indium content ~20-24% forming either side of a narrow region of lower indium content ~18%, with the latter coinciding with the apex of the now intersecting {1-100} planes.

Lu *et al.*[29] predicted that indium accumulates and segregates at the outer corners of hexagonal nanorods due to a release of strain energy through local deformation at these points in the nanostructure. The release of strain energy consequently leads to the segregation of indium to the corners. However, the initial InGaN shell growth takes place with the residual {11-20} planes retained leading to the observed indium distribution.

In addition to increasing the indium content, the release of strain energy may lead to the unintentional incorporation of point defects. These serve as non-radiative recombination centres [30–32] that may lead to the observed reduction in the luminescent intensity. Further optimisation of the facet overgrowth will aid in the development of more uniform and higher efficiency core-shell nanorods.

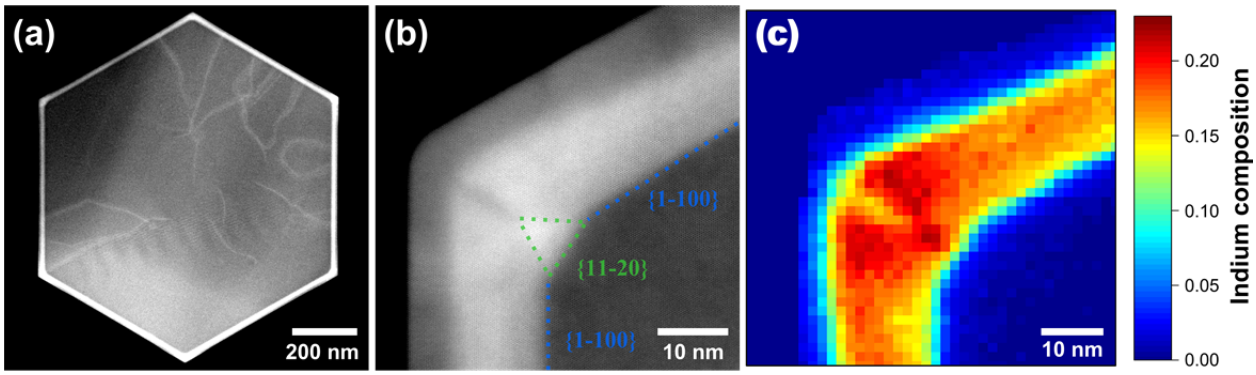


Figure 3. a) Atomic resolution ADF-STEM image of (a) a nanorod in cross-section viewed along the polar axis (b) higher resolution image of the upper left corner of a nanorod revealing the presence of a shrinking {11-20} facet. (c) The indium composition map showing the distribution of indium around the corner of a nanorod measured by EDS.

In conclusion, we have revealed the nanoscale optical and structural properties of InGaN core-shell nanorods. We have shown the fabrication of a uniform array of nanorods, with strong luminescent intensity arising from the non-polar {1-100} sidewalls. Nano-CL revealed a reduction in the luminescent intensity at the corners and there is a red-shift in emission energy that is most pronounced at the apex. Compositional analysis has revealed that the indium composition in general increases towards the corners of the nanorods and particularly at the tips in broad agreement with the predictions of Lu *et al*. but with an unpredicted reduction in the indium content at the apex itself. We propose that the red-shift in emission energy at the corners of the nanorods may arise from the increase in the indium composition and potential nanoscale variations in strain, whilst the reduction in luminescence may arise from the incorporation of point defects. Further optimisation of the nanostructure will aid the development of higher efficiency core-shell nanorods.

The authors would like to thank OSRAM Opto Semiconductors for the provision of the GaN/Silicon templates and acknowledge financial support from the European Union FP7 Contract No. 228999 (SMASH) and No. 279361 (MACONS) and the EPSRC, UK (EP/M015181/1 'Manufacturing of nanoengineered III Nitride semiconductors').

[1] J.W. Orton and C.T. Foxon, Reports Prog. Phys. **61**, 1 (1998).

[2] S. Pimputkar, J.S. Speck, S.P. DenBaars, and S. Nakamura, Nat. Photonics **3**, 180 (2009).

[3] C.J. Humphreys, MRS Bull. **33**, 459 (2011).

[4] F. Bernardini, V. Fiorentini, and D. Vanderbilt, Phys. Rev. B **56**, R10024 (1997).

[5] D.A.B. Miller, D.S. Chemla, and S. Schmitt-Rink, Phys. Rev. B **33**, 6976 (1986).

[6] G. Verzellesi, D. Saguatti, M. Meneghini, F. Bertazzi, M. Goano, G. Meneghesso, and E. Zanoni, J. Appl. Phys. **114**, 71101 (2013).

[7] J.S. Speck and S.F. Chichibu, MRS Bull. **34**, 304 (2011).

[8] P. Waltereit, O. Brandt, A. Trampert, H. Grahn, J. Menniger, M. Ramsteiner, M. Reiche, and K. Ploog, Nature **406**, 865 (2000).

[9] D. Sutherland, F. Oehler, T. Zhu, J.T. Griffiths, T.J. Badcock, P. Dawson, R.M. Emery, M.J. Kappers, C.J. Humphreys, and R.A. Oliver, Phys. Status Solidi C **114**, 541 (2014).

[10] J.R. Riley, S. Padalkar, Q. Li, P. Lu, D.D. Koleske, J.J. Wierer, G.T. Wang, and L.J. Lauhon, Nano Lett. **13**, 4317 (2013).

[11] H.M. Kim, Y.H. Cho, H. Lee, S.I.I. Kim, S.R. Ryu, D.Y. Kim, T.W. Kang, and K.S. Chung, Nano Lett. **4**, 1059 (2004).

[12] F. Qian, S. Gradečak, Y. Li, C.Y. Wen, and C.M. Lieber, Nano Lett. **5**, 2287 (2005).

[13] P.-M. Coulon, S.H. Vajargah, A. Bao, P.R. Edwards, E.D. Le Boulbar, I. Girgel, R.W. Martin, C.J. Humphreys, R.A. Oliver, D.W.E. Allsopp, and P.A. Shields, Cryst. Growth Des. **17**, 474 (2017).

[14] M. Heiss, Y. Fontana, A. Gustafsson, G. Wust, C. Magen, D.D. O'Regan, J.W. Luo, B. Ketterer, S. Conesa-Boj, A. V. Kuhlmann, J. Houel, E. Russo-Averchi, J.R. Morante, M. Cantoni, N. Marzari, J. Arbiol, A. Zunger, R.J. Warburton, and A. Fontcuberta i Morral, Nat. Mater. **12**, 439 (2013).

[15] M.J. Holmes, K. Choi, S. Kako, M. Arita, and Y. Arakawa, Nano Lett. **14**, 982 (2014).

[16] T.J. Puchtler, T. Wang, C.X. Ren, F. Tang, R.A. Oliver, R.A. Taylor, and T. Zhu, Nano Lett. **16**, 7779 (2016).

[17] J.T. Griffiths, S. Zhang, B. Rouet-Leduc, W.Y. Fu, A. Bao, D. Zhu, D.J. Wallis, A. Howkins, I. Boyd, D. Stowe, M.J. Kappers, C.J. Humphreys, and R.A. Oliver, Nano Lett. **15**, 7639 (2015).

[18] L.F. Zagonel, S. Mazzucco, M. Tencé, K. March, R. Bernard, B. Laslier, G. Jacopin, M. Tchernycheva, L. Rigutti, F.H. Julien, R. Songmuang, and M. Kociak, Nano Lett. **11**, 568 (2011).

[19] A. Urban, M. Müller, C. Karbaum, G. Schmidt, P. Veit, J. Malindretos, F. Bertram, J. Christen, and A. Rizzi, Nano Lett. **15**, 5105 (2015).

[20] X. Zhou, M.-Y. Lu, Y.-J. Lu, E.J. Jones, S. Gwo, and S. Gradečak, ACS Nano **9**, 2868 (2015).

[21] M. Muller, P. Veit, F.F. Krause, T. Schimpke, S. Metzner, F. Bertram, T. Mehrtens, K. Muller-Caspary, A. Avramescu, M. Strassburg, A. Rosenauer, and J. Christen, Nano Lett. **16**, 5340 (2016).

[22] P.A. Shields and D.W.E. Allsopp, Microelectron. Eng. **88**, 3011 (2011).

[23] E.D. Le Boulbar, I. Gîrgel, C.J. Lewins, P.R. Edwards, R.W. Martin, A. Šatka, D.W.E. Allsopp, and P.A. Shields, J. Appl. Phys. **114**, 94302 (2013).

[24] M.A. Reshchikov, D.O. Demchenko, A. Usikov, H. Helava, and Y. Makarov, Phys. Rev. B **90**, 235203 (2014).

[25] I. Gîrgel, P.R. Edwards, E. Le Boulbar, P.-M. Coulon, S.-L. Sahonta, D.W.E. Allsopp, R.W. Martin, C.J. Humphreys, and P.A. Shields, J. Nanophotonics **10**, 16010 (2016).

[26] E.D. Le Boulbar, P.R. Edwards, S.H. Vajargah, I. Griffiths, I. Gîrgel, P.-M. Coulon, D. Cherns, R.W. Martin, C.J. Humphreys, C.R. Bowen, D.W.E. Allsopp, and P.A. Shields, Cryst. Growth Des. **16**, 1907 (2016).

[27] J.T. Griffiths, S. Zhang, J. Lhuillier, D. Zhu, W.Y. Fu, A. Howkins, I. Boyd, D. Stowe, D.J. Wallis, C.J. Humphreys, and R.A. Oliver, J. Appl. Phys. **120**, 165704 (2016).

[28] B. Leung, Q. Sun, C.D. Yerino, J. Han, and M.E. Coltrin, Semicond. Sci. Technol. **27**, 24005 (2012).

[29] P.F. Lu, C. Sun, H.W. Cao, H. Ye, X.X. Zhong, Z.Y. Yu, L.H. Han, and S.M. Wang, Solid State Commun. **178**, 1 (2014).

[30] A.M. Armstrong, M.H. Crawford, and D.D. Koleske, Appl. Phys. Express **7**, 32101 (2014).

[31] E. Gür, Z. Zhang, S. Krishnamoorty, S. Rajan, and S.A. Ringel, Appl. Phys. Lett. **99**, 92109 (2011).

[32] A. Uedono, S. Ishibashi, N. Oshima, R. Suzuki, and M. Sumiya, ECS Trans. **61**, 19 (2014).

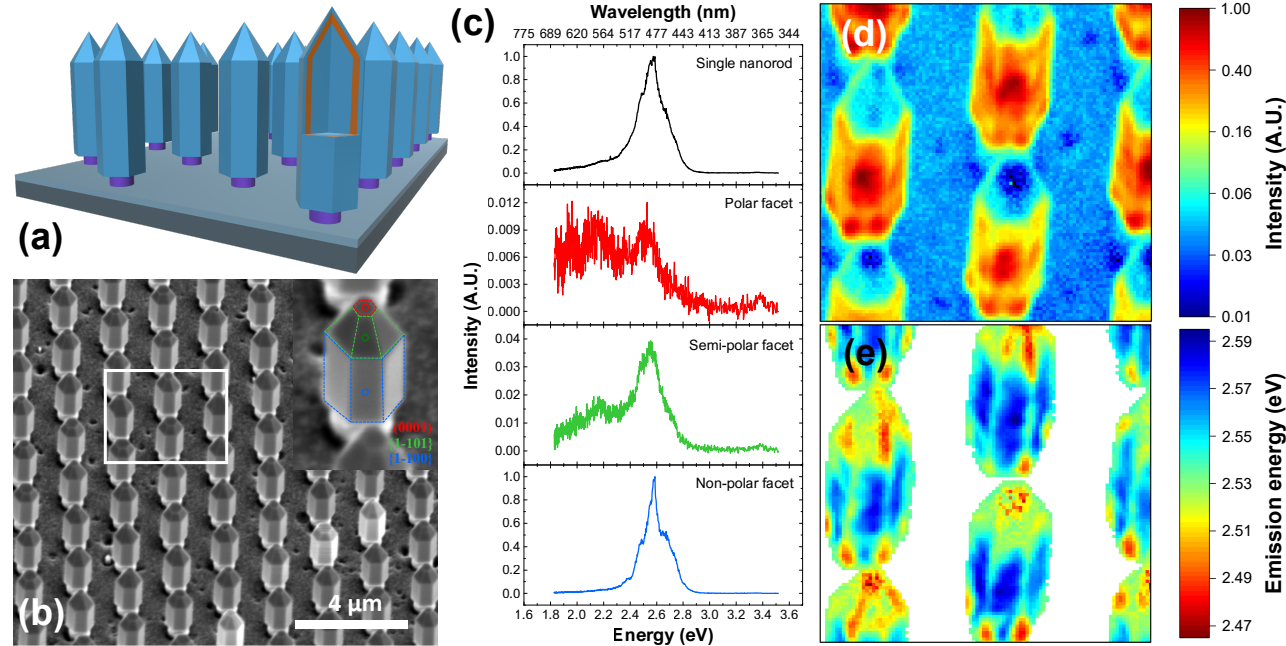
(a)
(b)
(0001)
(1-101)
(1-100)
4 μm
(c)
Wavelength (nm)
775 689 620 564 517 477 443 413 387 365 344
Single nanorod
Polar facet
Semi-polar facet
Non-polar facet
Intensity (A.U.)
Energy (eV)
(d)
(e)
Intensity (A.U.)
Emission energy (eV)

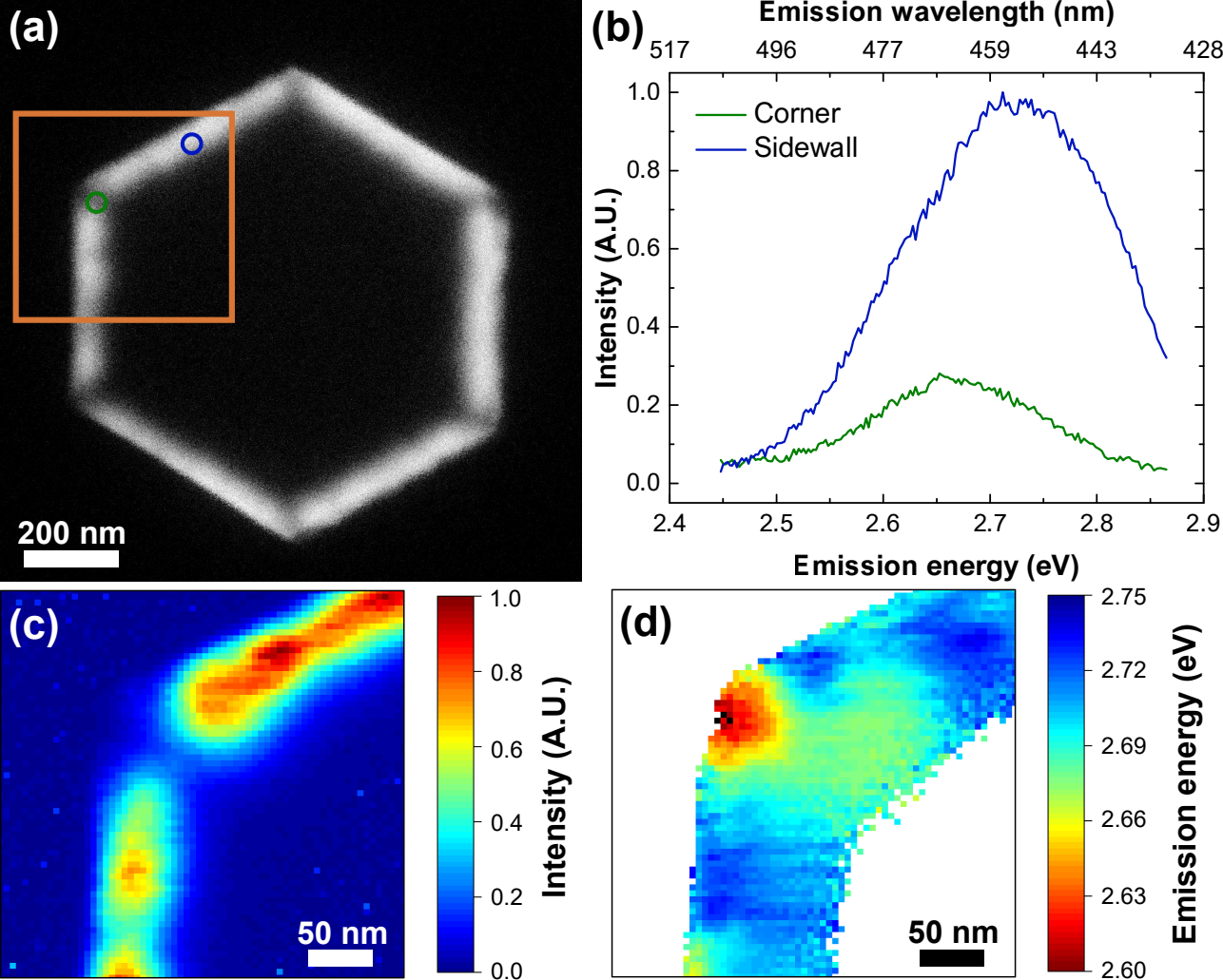
(a)
200 nm
(b)
Emission wavelength (nm)
517
496
477
459
443
428
Corner
Sidewall
Intensity (A.U.)
1.0
0.8
0.6
0.4
0.2
0.0
2.4
2.5
2.6
2.7
2.8
2.9
Emission energy (eV)
(c)
50 nm
1.0
0.8
0.6
0.4
0.2
0.0
Intensity (A.U.)
(d)
50 nm
2.75
2.72
2.69
2.66
2.63
2.60
Emission energy (eV)

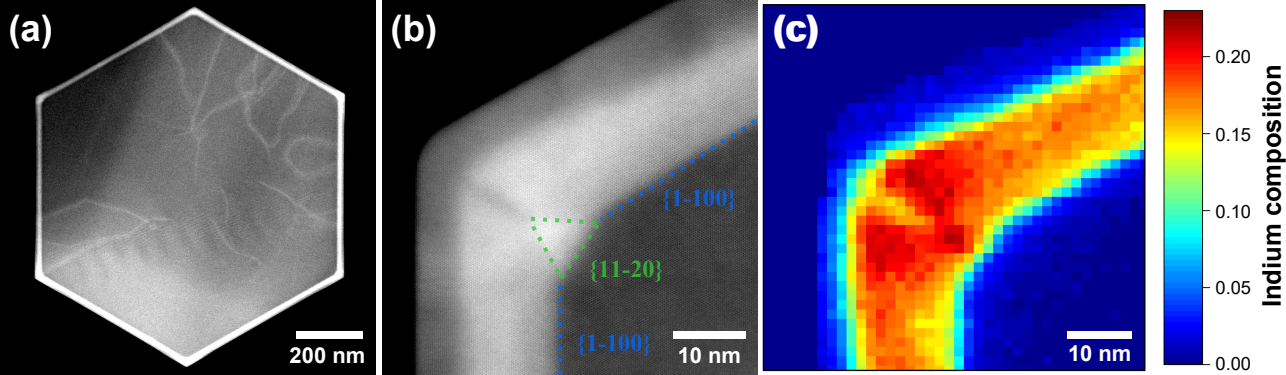
(a)
200 nm
(b)
{1-100}
{11-20}
{1-100}
10 nm
(c)
10 nm
0.20
0.15
0.10
0.05
0.00
Indium composition